Elastic least-squares reverse time migration using the energy norm

Daniel Rocha & Paul Sava
Center for Wave Phenomena, Colorado School of Mines

SUMMARY

We derive linearized modeling and migration operators based on the energy norm for elastic wavefields in arbitrary anisotropic media. We use these operators to perform anisotropic least-squares reverse time migration (LSRTM) and generate a scalar image that represents subsurface reflectivity without costly decomposition of wave modes. Imaging operators based on the energy norm have the advantage of removing backscattering artifacts, thus accelerating convergence and generating images of higher quality. With synthetic and field data experiments, we show that our LSRTM method is suitable to generate images that correctly predict observed data without the complexity of wave-mode decomposition in arbitrary anisotropic media.

INTRODUCTION

The search for more reliable seismic images and subsurface information, such as fracture distribution, drives advances in seismic acquisition towards larger offsets, wider azimuth coverage and multicomponent recording. These advances facilitate incorporating anisotropy and elasticity into wavefield extrapolation and reverse time migration (RTM) (Baysal et al., 1983; McMechan, 1983; Lailly, 1983; Chang and McMechan, 1987; Hokstad et al., 1998). However, acquisition always has practical limitations, such as finite and irregular data sampling, that negatively impact anisotropic elastic wavefield migration. Consequently, this type of migration often leads to images with poor resolution and unbalanced illumination due to such acquisition constraints, even though image amplitudes are more reliable compared to acoustic and/or isotropic imaging (Lu et al., 2009; Phadke and Dhubia, 2012; Hobro et al., 2014; Du et al., 2014).

A common solution to these limitations is least-squares reverse time migration (LSRTM), which attenuates artifacts caused by truncated acquisition and provides images that best predict observed data (Chavent and Plessix, 1999; Nemeth et al., 1999; Kuhl and Sacchi, 2003; Aoki and Schuster, 2009; Yao and Jakubowicz, 2012; Dong et al., 2012). Some authors propose LSRTM that accounts for a multiparameter Earth model, which can either incorporate anisotropic, elastic, or attenuation effects. For instance, visco-acoustic and pseudo-acoustic implementations define Earth reflectivity in terms of contrast from a single model parameter (Dutta and Schuster, 2014; Huang et al., 2016) or in terms of a scalar image based on conventional correlation between wavefields (Sun et al., 2015). Alternatively, elastic LSRTM implementations in isotropic media provide multiple images that are defined in terms of correlation between decomposed wave modes (Duan et al., 2016; Feng and Schuster, 2016; Xu et al., 2016; Alves and Biondi, 2016). However, wave-mode decomposition in anisotropic media is costly and not as straightforward as in isotropic media, and remains subject of ongoing research (Zhang and McMechan, 2010; Yan and Sava, 2011; Cheng and Fomel, 2014; Sripanich et al., 2015; Wang et al., 2016).

Elastic wavefield imaging using the energy norm (Rocha et al., 2017) exploits realistic vector wavefield extrapolation in a multiparameter anisotropic and elastic Earth model, and generates a scalar image without costly decomposition of wave modes. This imaging condition exhibits no polarity reversal at normal incidence, and computes an appropriate correlation between wavefields that attenuates low-wavenumber artifacts caused by waves that do not correctly characterize subsurface reflectivity (e.g. wave backscattering from salt interfaces). We interpret the resulting amplitudes as a measure of energy transfer between incident and reflected wavefields. As for any other wavefield migration method, its quality suffers from the acquisition limitations discussed earlier. Therefore, we propose a LSRTM method using the energy image as the reflectivity model and defining a linearized modeling operator that generates anisotropic elastic scattered wavefields.

THEORY

We can express elastic wavefield migration as

$$\mathbf{m} = \mathbf{L}^{\mathrm{T}}\mathbf{d}_r \ , \tag{1}$$

where $\mathbf{L}^{\mathrm{T}}$ is the migration operator, $\mathbf{d}_r$ is single-scattered multicomponent data recorded at receiver locations, and $\mathbf{m}$ is an image associated with the Earth reflectivity. The operator $\mathbf{L}^{\mathrm{T}}$ involves backpropagation of $\mathbf{d}_r$ through an Earth model generating a receiver wavefield $\mathbf{U}_r$, and the application of an imaging condition comparing $\mathbf{U}_r$ with the source wavefield $\mathbf{U}_s$. One generally considers migration as the adjoint operator of linearized modeling (Claerbout, 1992), which is expressed by

$$\mathbf{d}_r = \mathbf{L}\mathbf{m} \ , \tag{2}$$

and generates scattered data $\mathbf{d}_r$ at receiver locations using an image containing reflectors that act as sources under the action of the background wavefield $\mathbf{U}_s$. Therefore, we define $\mathbf{m}$ as reflectivity that depends on a particular imaging condition and is not necessarily defined in terms of contrasts in the Earth model. The same principle applies to the modeling operator $\mathbf{L}$, which we define as an adjoint of a specific migration operator.

For anisotropic elastic source and receiver wavefields, functions of space and time ($\mathbf{U}_s(\mathbf{x},t)$ and $\mathbf{U}_r(\mathbf{x},t)$), the energy imaging condition is (Rocha et al., 2017)

$$\mathbf{m}(\mathbf{x}) = \sum_t \left[\rho\dot{\mathbf{U}}_s \cdot \dot{\mathbf{U}}_r + \left(\underline{\underline{\mathbf{c}}}\nabla\mathbf{U}_s\right) : \nabla\mathbf{U}_r\right] , \tag{3}$$

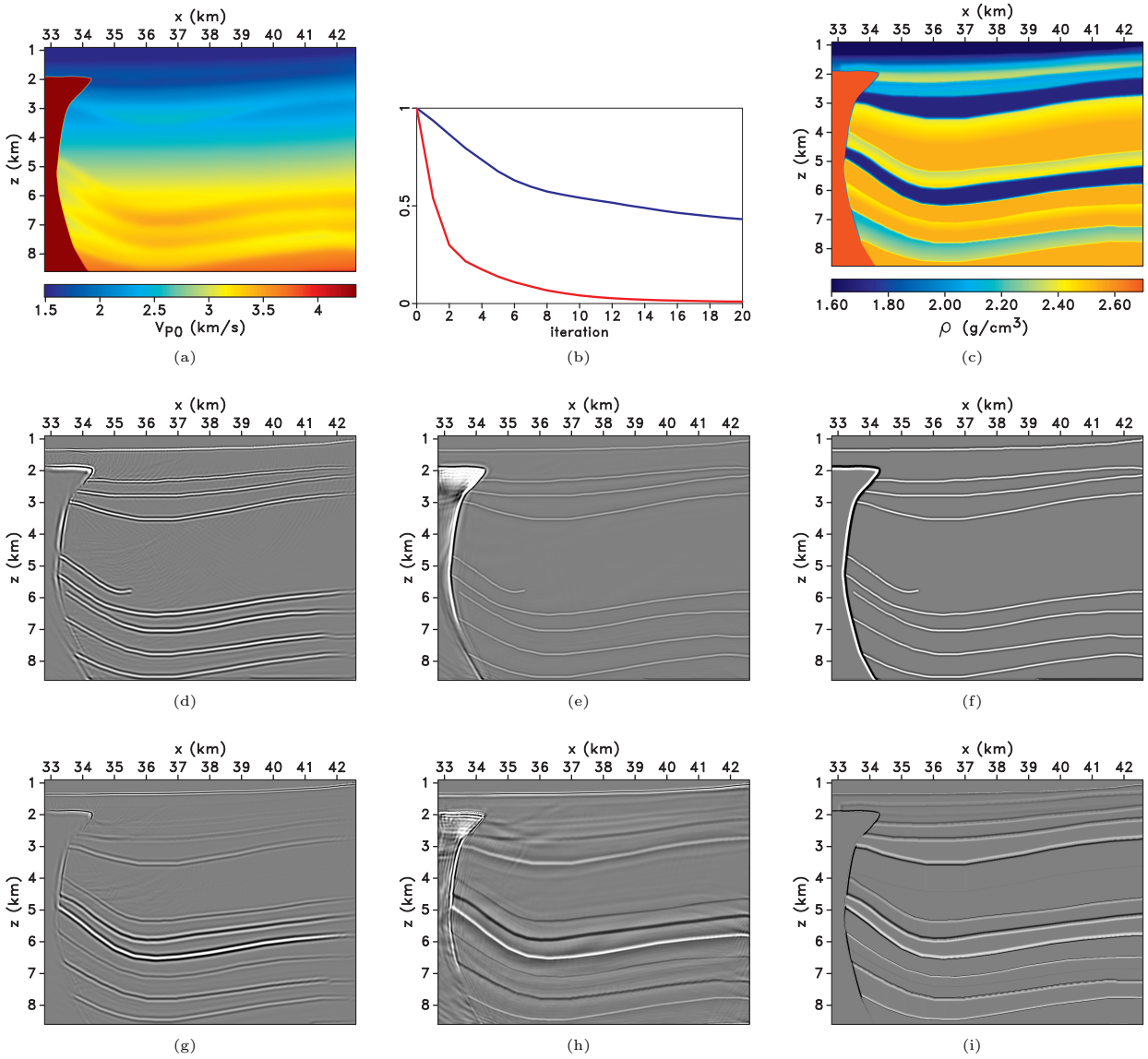

Figure 1: BP TTI experiment: (a) V_{P0} model, (b) normalized objective function for energy LSRTM using full-modeled data (blue) and linearized-modeled data (red), (c) density with contrasts for full-wavefield modeling. RTM and LSRTM images using (d)/(e) linearized-modeled data and (g)/(h) full-modeled data. (f) True reflectivity model for linearized-modeled data and (i) Laplacian operator applied on the density model in Figure 1c to show contrasts that create reflections during full-wavefield modeling. Compared to the RTM images, the LSRTM images show sharper reflectors and more balanced illumination, especially at the salt flanks.

where $\rho(\mathbf{x})$ is the density and $\underline{\mathbf{c}}$ is the second-order stiffness tensor. The superscript dot applied on the wavefields indicates time differentiation and ∇ is the spatial gradient. The symbol : indicates the Frobenius product between two matrices resulting in a scalar (Golub and Loan, 1996). A more compact form of equation 3 utilizes the energy vectors, defined as

$$\square\mathbf{U}_{s,r} = \left\{\rho^{1/2}\dot{\mathbf{U}}_{s,r}, \underline{\mathbf{c}}^{1/2}\nabla\mathbf{U}_{s,r}\right\} , \tag{4}$$

for source (s) and receiver (r) wavefields, respectively. Using the definition of energy vectors from equation 4, the imaging condition in equation 3 becomes

$$\mathbf{m} = \left(\square\mathbf{U}_s\right)^{\mathrm{T}} \square\mathbf{U}_r \ . \tag{5}$$

We can write the elastic wavefields $\mathbf{U}_s$ and $\mathbf{U}_r$ in terms of a sequence of operators applied to the source function $\mathbf{d}_s$ and to the receiver data $\mathbf{d}_r$, respectively. Firstly, we implement injection of the source function and receiver data into the Earth model by operators $\mathbf{K}_s$ and $\mathbf{K}_r$, respectively. Secondly, we apply forward and backward

elastic wavefield extrapolation operators $\mathbf{E}_+$ and $\mathbf{E}_-$, respectively. Hence, we can rewrite $\mathbf{m} = \mathbf{L}^{\mathrm{T}}\mathbf{d}_r$ with

$$\mathbf{L}^{\mathrm{T}} = (\square\mathbf{E}_+\mathbf{K}_s\mathbf{d}_s)^{\mathrm{T}}\,\square\mathbf{E}_-\mathbf{K}_r = (\square\mathbf{U}_s)^{\mathrm{T}}\,\square\mathbf{E}_-\mathbf{K}_r\ . \quad (6)$$

Therefore, the chain of operators in equation 6 represents migration based on the energy norm. Similarly to equation 2, we express the operator $\mathbf{L}$ (adjoint of $\mathbf{L}^{\mathrm{T}}$) as

$$\mathbf{L} = \mathbf{K}_r^{\mathrm{T}}\mathbf{E}_+\square^{\mathrm{T}}\,(\square\mathbf{E}_+\mathbf{K}_s\mathbf{d}_s) = \mathbf{K}_r^{\mathrm{T}}\mathbf{E}_+\square^{\mathrm{T}}\square\mathbf{U}_s\ . \quad (7)$$

The chain of operators in equation 7 represents modeling based on the energy norm, involving extraction of multicomponent single-scattered data at the receiver locations using operator $\mathbf{K}_r^{\mathrm{T}}$, and elastic wavefield extrapolation ($\mathbf{E}_+$) from virtual multicomponent sources $\square^{\mathrm{T}}\square\mathbf{U}_s\mathbf{m}$.

To summarize, the steps involved in computing the scattered data $\mathbf{d}_r$ with the energy norm are:

1. Extrapolate ($\mathbf{E}_+$) the background wavefield from the injected source $\mathbf{K}_s\mathbf{d}_s$;
2. Compute the virtual source $\square^{\mathrm{T}}\square\mathbf{U}_s\mathbf{m}$;
3. Extrapolate ($\mathbf{E}_+$) the virtual source and extract the resulting wavefield at receiver locations ($\mathbf{K}_r^{\mathrm{T}}$).

Then, the linearized modeling operator $\mathbf{L}$ and its adjoint enables us to compute an image $\mathbf{m}$ that minimizes the objective function

$$E\,(\mathbf{d},\mathbf{m}) = \frac{1}{2}\|\mathbf{L}\mathbf{m} - \mathbf{d}_r\|^2\ , \quad (8)$$

which represents LSRTM with the energy norm.

EXAMPLES

We demonstrate our method using a portion of the 2007 BP TTI benchmark model. The original model consists of V_{P0}, ϵ, δ, and the tilt of the symmetry axis (ν); we create V_{S0} and ρ from the other parameters (Figures 1a and 1c). The experiment geometry consists of 55 pressure sources equally spaced in the water at the surface ($z = 0.092$km), and a line of multicomponent receivers at every grid point at the water bottom, whose depth varies between $z = 1.0$km and $z = 1.4$km. We generate two different datasets by (a) full-wavefield modeling, using the density model with contrasts (Figure 1c), and (b) linearized modeling, using a constant density model and the reflectivity model in Figure 1f to generate reflections. All other Earth model parameters are kept the same between the two experiments. We obtain energy RTM and LSRTM images using linearized-modeled data (Figures 1d and 1e) and full-modeled data (Figures 1g and 1h). We apply an exponential gain with depth on the RTM images for a fair comparison with LSRTM images. Notice that artifacts (mainly caused by the incomplete acquisition) in the shallow part of the model are attenuated, and the salt flanks are better illuminated in the LSRTM images compared to their RTM counterparts. Both LSRTM images are closer to the assumed true reflectivity models shown in Figures 1f and 1i. For the LSRTM images, one can observe low-wavenumber artifacts inside the salt because most of the waves in this region do not scatter towards the receivers due to the experiment geometry. These events create artifacts that accumulate over iterations, and they constitute the null space of the inversion, i.e., they do not predict any reflections in the data. Although such artifacts do not represent actual reflectors, they are not harmful to the inversion since they reside in the null space of the reflectivity model and do not mask any reflectors inside the salt body. The objective functions for both experiments are shown in Figure 1b, and as expected, the objective function for the data generated by the linearized modeling operator itself converges to zero as our migration and modeling operators are proper adjoints. The objective function for the experiment with full-modeled data decreases substantially and could decrease further if more iterations are allowed, since the objective function at iteration 20 retains a significant slope as seen in Figure 1b. However, we expect the rate of convergence to diminish over iterations until the objective function reaches a plateau, because our modeling operator cannot predict events beyond single scattering.

We apply the method on a field dataset acquired by an ocean-bottom cable (OBC) survey in the Volve field, located in the North Sea (Szydlik et al., 2007). Although the original dataset is 3D, we use a 2D section near the central crossline to reduce computational cost. The Earth model is elastic VTI (Figure 2). The prominent reflector around $z = 3$ km is a chalk layer that corresponds to the reservoir. The dataset was preprocessed to retain only the down-going pressure component (Figure 3a). We obtain energy RTM and LSRTM images (after 15 iterations), shown in Figures 4a and Figure 4b, and the corresponding objective function in Figure 3c. The LSRTM image presents more detailed reflectors compared to the RTM image, and enhances the amplitudes at the edges of the model. By comparing the modeled data at the last iteration (Figure 3b) and the observed data (Figure 3a), one can note that our linearized modeling operator and the image at the last iteration predict the main reflections and do not predict events such as noise, direct arrival, far-offset amplitudes, etc.

CONCLUSIONS

We propose a LSRTM method that uses imaging operators based on the energy norm and delivers a scalar image that contains attenuated artifacts and explains data at receiver locations. The absence of strong backscattering artifacts in our results shows the advantage of our migration operator compared to its conventional counterparts. Using displacement fields directly and without costly wave-mode decomposition, our modeling operator generates multicomponent datasets with a scalar reflectivity that correctly predicts the reflections on the observed data, as seen in the final modeled data and

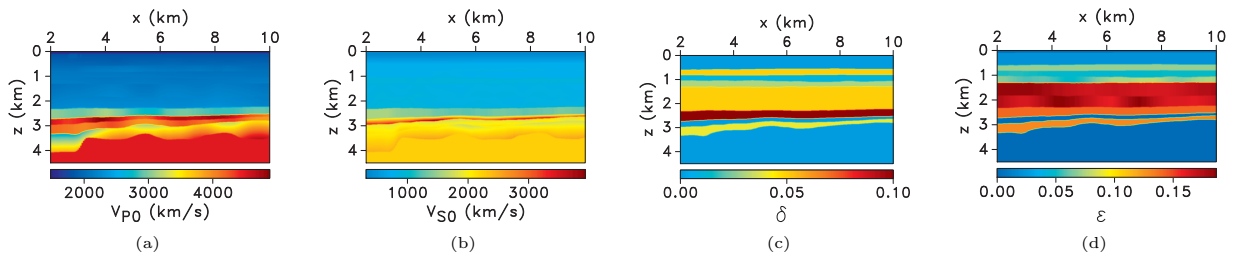

Figure 2: Volve Earth model: vertical (a) P-wave and (b) S-wave velocities; Thomsen parameters (c) δ and (d) ϵ.

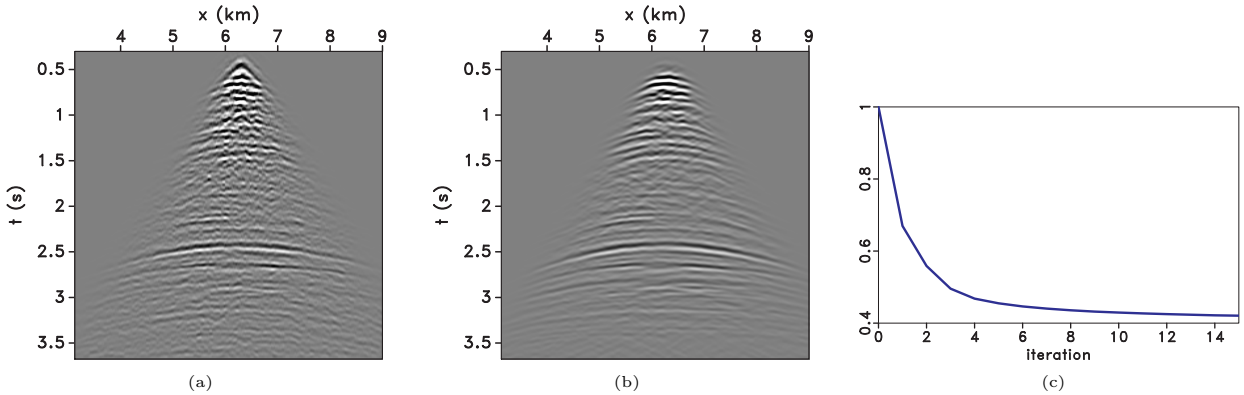

Figure 3: Volve experiment: (a) observed and (b) modeled (after 15 iterations) shot gathers for a source at $x = 6.4$km. Comparing the two gathers, note the reflection events predicted by our modeling operator. (c) Normalized objective function for LSRTM.

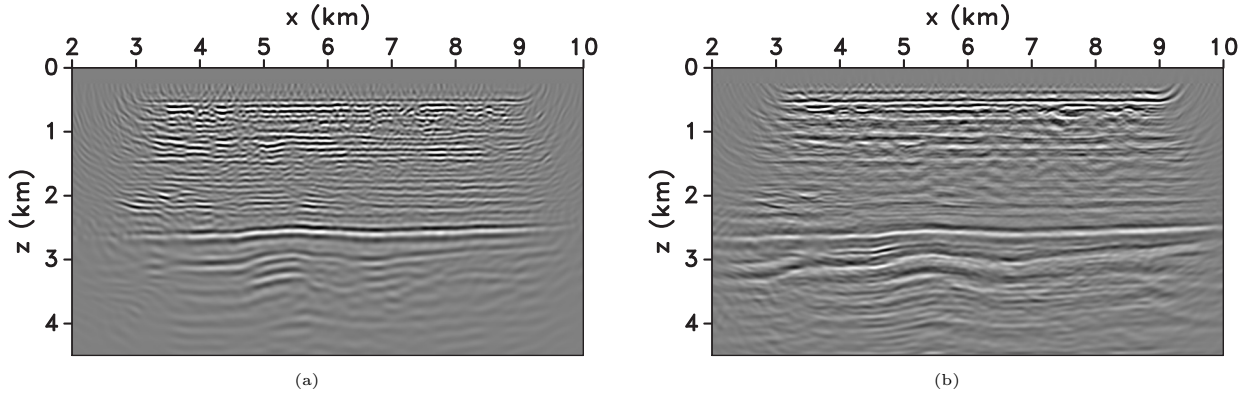

Figure 4: Volve experiment: energy (a) RTM and (b) LSRTM images. Reflectors around $z = 3.0$km have more detail, especially at the edges of the image.

objective functions from our examples.

ACKNOWLEDGEMENTS

We thank the sponsors of the Center for Wave Phenomena, whose support made this research possible. We acknowledge Hemang Shah and BP Exploration Operation Company Limited for creating the TTI model. We thank Statoil ASA and the Volve license partners ExxonMobil E&P Norway AS and Bayerngas Norge AS for the release of the Volve data. We acknowledge Antoine Guitton for helpful discussions. The synthetic examples in this paper use the Madagascar open-source software package (Fomel et al., 2013) freely available from http://www.ahay.org.

REFERENCES

Alves, G., and B. Biondi, 2016, Imaging condition for elastic reverse time migration: Presented at the 86th Annual International Meeting, SEG, Expanded Abstracts, 3959–3965.

Aoki, N., and G. T. Schuster, 2009, Fast least-squares migration with a deblurring filter: Geophysics, **74**, no. 6, WCA83–WCA93.

Baysal, E., D. D. Kosloff, and J. W. C. Sherwood, 1983, Reverse time migration: Geophysics, **48**, 1514–1524.

Chang, W.-F., and G. A. McMechan, 1987, Elastic reverse-time migration: Geophysics, **52**, 1365–1375.

Chavent, G., and R.-E. Plessix, 1999, An optimal true–amplitude least–squares prestack depth–migration operator: Geophysics, **64**, 508–515.

Cheng, J., and S. Fomel, 2014, Fast algorithms for elastic-wave-mode separation and vector decomposition using low-rank approximation for anisotropic media: Geophysics, **79**, no. 4, C97–C110.

Claerbout, J. F., 1992, Earth soundings analysis: Processing versus inversion: Blackwell Scientific Publications.

Dong, S., J. Cai, M. Guo, S. Suh, Z. Zhang, B. Wang, and Z. Li, 2012, Least-squares reverse time migration: towards true amplitude imaging and improving the resolution: Presented at the 82rd Annual International Meeting, SEG, Expanded Abstracts.

Du, Q., M. Zhang, G. Fang, X. Gong, and C. Guo, 2014, Relatively amplitude-preserved ADCIGs based on elastic RTM by modifying the initial condition as the boundary condition: Presented at the 84th Annual International Meeting, SEG, Expanded Abstracts, 1888–1893.

Duan, Y., P. Sava, and A. Guitton, 2016, Elastic least-squares reverse time migration: Presented at the 86th Annual International Meeting, SEG, Expanded Abstracts, 3959–3965.

Dutta, G., and G. T. Schuster, 2014, Attenuation compensation for least-squares reverse time migration using the viscoacoustic-wave equation: Geophysics, **79**, no. 6, S251–S262.

Feng, Z., and G. T. Schuster, 2016, Elastic least-squares reverse time migration: Presented at the 86th Annual International Meeting, SEG, Expanded Abstracts, 3959–3965.

Fomel, S., P. Sava, I. Vlad, Y. Liu, and V. Bashkardin, 2013, Madagascar: open-source software project for multidimensional data analysis and reproducible computational experiments: Journal of Open Research Software, 1:e8, DOI: http://dx.doi.org/10.5334/jors.ag.

Golub, G. H., and C. F. V. Loan, 1996, Chapter 2 - Matrix Analysis, *in* Matrix computations, 3rd ed.: John Hopkins University Press.

Hobro, J. W. D., C. H. Chapman, and J. O. A. Robertsson, 2014, A method for correcting acoustic finite-difference amplitudes for elastic effects: Geophysics, **79**, no. 4, T243–T255.

Hokstad, K., R. Mittet, and M. Landrø, 1998, Elastic reverse time migration of marine walkaway vertical seismic profiling data: Geophysics, **63**, 1685–1695.

Huang, J., D. Si, Z. Li, and J. Huang, 2016, Plane-wave least-squares reverse time migration in complex VTI media: Presented at the 86th Annual International Meeting, SEG, Expanded Abstracts, 441–446.

Kuhl, H., and M. D. Sacchi, 2003, Least-squares wave-equation migration for AVO/AVA inversion: Geophysics, **68**, 262–273.

Lailly, P., 1983, The seismic inverse problem as a sequence of before stack migrations: Conference on Inverse Scattering, Theory and Application: Presented at the Society of Industrial and Applied Mathematics, Expanded Abstracts, 206–220.

Lu, R., P. Traynin, and J. E. Anderson, 2009, Comparison of elastic and acoustic reverse–time migration on the synthetic elastic Marmousi–II OBC dataset: Presented at the 79th Annual International Meeting, SEG, Expanded Abstracts, 2799–2803.

McMechan, G. A., 1983, Migration by extrapolation of time dependent boundary values: Geophysical Prospecting, **31**, 413–420.

Nemeth, T., C. Wu, and G. T. Schuster, 1999, Least–squares migration of incomplete reflection data: Geophysics, **64**, 208–221.

Phadke, S., and S. Dhubia, 2012, Reverse time migration of marine models with elastic wave equation and amplitude preservation: Presented at the 82nd Annual International Meeting, SEG, Expanded Abstracts.

Rocha, D., N. Tanushev, and P. Sava, 2017, Anisotropic elastic wavefield imaging using the energy norm: Geophysics, **82**, no. 3, S225–S234.

Sripanich, Y., S. Fomel, J. Sun, and J. Cheng, 2015, Elastic wave-vector decomposition in orthorhombic media: Presented at the 85th Annual International Meeting, SEG, Expanded Abstracts, 498–503.

Sun, J., S. Fomel, and T. Zhu, 2015, Preconditioning least-squares RTM in viscoacoustic media by Q-compensated RTM: Presented at the 85th Annual International Meeting, SEG, Expanded Abstracts, 3959–3965.

Szydlik, T., P. Smith, S. Way, L. Aamodt, and C. Friedrich, 2007, 3d pp/ps prestack depth migration on the volve field: First Break, **25**, no. 4, 4347.

Wang, W., G. A. McMechan, C. Tang, and F. Xie, 2016, Up/down and P/S decompositions of elastic wavefields using complex seismic traces with applications to calculating Poynting vectors and angle-domain common-image gathers from reverse time migrations: Geophysics, **81**, no. 4, S181–S194.

Xu, L., A. Stanton, and M. D. Sacchi, 2016, Elastic least squares reverse time migration: Presented at the 86th Annual International Meeting, SEG, Expanded Abstracts, 3959–3965.

Yan, J., and P. Sava, 2011, Elastic wave-mode separation for tilted transverse isotropy media: Geophysical Prospecting, **60**, 29–48.

Yao, G., and H. Jakubowicz, 2012, Least-Squares Reverse-Time Migration: Presented at the 82rd Annual International Meeting, SEG, Expanded Abstracts.

Zhang, Q., and G. A. McMechan, 2010, 2D and 3D elastic wavefield vector decomposition in the wavenumber domain for VTI media: Geophysics, **75**, D13–D26.